3-D Path-Following Control for Steerable Needles with Fiber Bragg Gratings in Multi-Core Fibers

Abdulhamit Donder and Ferdinando Rodriguez y Baena, *Member, IEEE*

Abstract—Steerable needles have the potential for accurate needle tip placement even when the optimal path to a target tissue is curvilinear, thanks to their ability to steer, which is an essential function to avoid piercing through vital anatomical features. Autonomous path-following controllers for steerable needles have already been studied, however they remain challenging, especially because of the complexities associated to needle localization. In this context, the advent of fiber Bragg Grating (FBG)-inscribed multi-core fibers (MCFs) holds promise to overcome these difficulties. *Objective:* In this study, a closed-loop, 3-D path-following controller for steerable needles is presented. *Methods:* The control loop is closed via the feedback from FBG-inscribed MCFs embedded within the needle. The nonlinear guidance law, which is a well-known approach for path-following control of aerial vehicles, is used as the basis for the guidance method. To handle needle-tissue interactions, we propose using Active Disturbance Rejection Control (ADRC) because of its robustness within hard-to-model environments. We investigate both linear and nonlinear ADRC, and validate the approach with a Programmable Bevel-tip Steerable Needle (PBN) in both phantom tissue and *ex vivo* brain, with some of the experiments involving moving targets. *Results:* The mean, standard deviation, and maximum absolute position errors are observed to be 1.79 mm, 1.04 mm, and 5.84 mm, respectively, for 3-D, 120 mm deep, path-following experiments. *Conclusion:* MCFs with FBGs are a promising technology for autonomous steerable needle navigation, as demonstrated here on PBNs. *Significance:* FBGs in MCFs can be used to provide effective feedback in path-following controllers for steerable needles.

Index Terms—FBG, fiber Bragg grating, steerable needles, PBN, programmable bevel-tip steerable needle, path-following controller, soft robotics, tumor surgery

I. INTRODUCTION

PERCUTANEOUS intervention is a kind of minimally invasive surgery that can provide important intra- and post-operative advantages, such as less pain and reduced recovery time, when compared to its open-surgery counterparts, [1]. Needle insertion is a typical example of percutaneous intervention, which is used extensively, for instance in brachytherapy [2], drug delivery [3], biopsy [4] and thermal ablation [5]. Steerable needles are a promising tool for needle insertion and have been studied widely by many research groups for the last two decades. A steerable needle is a needle that is able to steer during navigation in soft tissue, such as brain and liver, to avoid specific anatomical features (obstacles), such as veins and arteries. When compared to conventional rigid needles, their ability to steer enables successful operations even in the absence of a suitable straight path to the target tissue, which makes steerable needles

Abdulhamit Donder is with the Mechatronics in Medicine Laboratory, Department of Mechanical Engineering, Imperial College London, London SW7 2AZ, U.K., and also with the Department of Cardiovascular Surgery, Boston Children's Hospital, Harvard Medical School, Boston 02115, MA, USA (e-mail: abdulhamit.donder@childrens.harvard.edu)

Ferdinando Rodriguez y Baena is with the Mechatronics in Medicine Laboratory, Department of Mechanical Engineering, Imperial College London, London SW7 2AZ, U.K. (e-mail: f.rodriguez@imperial.ac.uk)
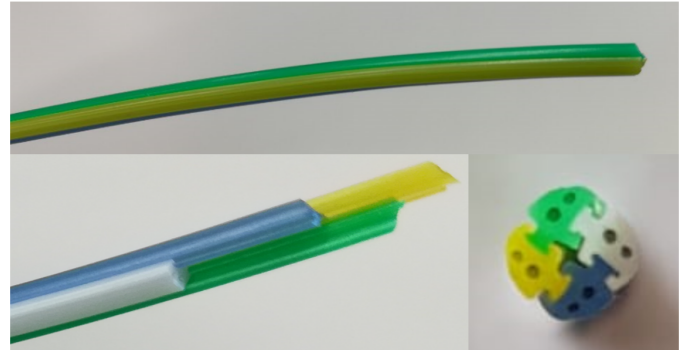

Fig. 1. A 4-segment Programmable Bevel-tip Steerable Needle (PBN). Top: Overall appearance with zero relative offsets between PBN segments, Bottom left: PBN-tip close-up with non-zero relative offsets between PBN segments, Bottom-right: PBN front-view, illustrating two hollow lumens per segment

a potential game-changer in many surgical procedures. In addition to obstacle avoidance, steerable needles are useful also in the case where the target tissue moves because of tissue deformation during the insertion process. In such cases, steerable needles provide the possibility to maneuver towards the new location of the target tissue. Therefore, they decrease (i) the need for reinsertion, which increases tissue-trauma [6], (ii) the risk of false diagnosis and ineffective therapy due to, for example, a biopsy being collected from or a drug being delivered to the wrong location [7].

Several steerable needle designs have been proposed to date, such as bevel-tip steerable needles [8], concentric tube needles [9], [10], tendon-driven steerable needles [11], and programmable bevel-tip steerable needles (PBNs) [12]. Bevel-tip steerable needles, which are often made of flexible materials, are the earliest type of steerable needle and have a fixed bevel-tip angle to steer with a constant curvature. Despite being simple-to-use on a fixed bending plane, they require the entire needle body to spin around the insertion axis to steer in another plane, which causes torsional moment on the surrounding tissue [13]. Although some variants decrease the possible tissue damage due to this effect with a flexible cannula over the stylet body [14], this type of needle still requires constant rotation to achieve a straight path [15], which may result in helical paths and increased tissue damage. Secondly, concentric tube needles are telescopically-combined elastic tubes, which do not require a rotation of the needle body in contact with the tissue. However, since the tubes are pre-curved, and there is not much room to update the pre-planned path, they are not tolerant to tissue movements and target tissue migration. Tendon driven steerable needles possess an active tip driven from the base via tendons. To change the steering direction, these needles require their articulated tip to move, which causes tissue displacement and might result in trauma. On the other hand, the programmable bevel-tip steerable needle (PBN), which is a bio-inspired soft needle (and used in this study), is inspired by wasps that use their slender ovipositors to penetrate into and steer through some substrates, such as wood, to lay their eggs [16]. Its soft, slender segments are interlaced together via an interlocking

mechanism. The PBN consists of at least 3 segments which can be driven independently to "program" the needle's tip in order to achieve the desired curvature vector, i.e., curvature value and bending direction, by exploiting the interaction forces with tissue. The main advantages of PBNs over the other well-known steerable needles can be summarized as follows: (i) PBNs are magnetic-resonance-imaging-compatible, (ii) the steering direction can be set to any direction in the 3-D space without the need to rotate the entire needle body [17], (iii) the reciprocal motion of the PBN segments decreases tissue deformation at the needle-tissue interface, [18], (iv) the steering ability can be increased with compliant PBN materials because of the absence of the need for the transmission of torque from base to tip, as in the case of duty cycle spinning [15]. A 4-segment PBN is shown in Fig. 1.

Although steerable needles provide the ability to steer, this is not enough for accurate needle tip placement. Efficient guidance control, by either a human or a computerized controller, must also be in place. However, the needle-tissue interaction is highly unpredictable because of several anatomical reasons, such as tissue heterogeneity, boundaries of tissue layers, bleeding, all of which lead to difficulties in constructing an accurate mathematical model and a computerized controller. The approaches proposed so far to control the 3-D navigation of steerable needles through a predefined path include sliding mode control [19]–[21], model predictive control [22], and fuzzy logic [23]. Among these, fuzzy and sliding mode controllers distinguish with their ability to deal with uncertainties. Sliding mode control, which was already used to control a PBN, is not ideal considering its long settling time [19]. On the other hand, fuzzy control is mainly based on human perception and experience, and controlling complex systems like PBN controllers require strong intuition for controller optimization.

Therefore, despite the growing amount of research over the last decade, accurate guidance of steerable needles is still an open research challenge. Also, with regards to 3-D path-following controllers of PBNs, there are only two studies in the literature [19], [24], and neither offers experimental validation. In these studies, the PBN tip is proposed to be programmed while the overall PBN advancement continues moving. We postulate that this approach might result in significant overshoot in the case of bending angle discontinuities because of the PBN moving forward before the offsets are suitably programmed.

In this study, we propose that the PBN advances after the completion of the PBN tip programming process at each step. To account for PBN-tissue interactions, the active disturbance rejection controller (ADRC) [25] is chosen as the control method, as it is known for its parameters having a wide adaptive range and its robustness even in the presence of a rough mathematical model of the system. The performance of ADRCs was shown previously using systems with unknown dynamics in hard-to-model environments, such as underwater vehicles [26], aerial vehicles [27], and autonomous grinding applications [28]. This control method is based on defining unmodeled dynamics and disturbances ("total disturbance") as the extended state in addition to the system states and estimating them via the Extended State Observer (ESO). The estimated generalized disturbance is canceled via a feedback controller, which helps transforming advanced control problems into simpler ones. In this study we investigated both the nonlinear ADRC (NADRC), which includes nonlinear functions in the ESO, and the linear ADRC (LADRC), of which the ESO consists of linear functions. In terms of high-level control, to guide the needle along the desired path, a controller based on nonlinear guidance law (NLGL) [29] has been designed. This is a control method commonly used for path following of fixed-wing unmanned aerial vehicles [30], which has the same nonholonomic

constraints as steerable needles including PBNs [19]. Furthermore, we propose, for the first time, an algorithm for programming the PBN tip while observing the permissibility condition of PBNs, i.e., a condition ensuring that the PBN acts as a single body at all times.

Among steerable needle controllers, a significant majority of studies used electromagnetic sensors, ultrasound sensors, and cameras for the localization of the needle tip. On the other hand, although FBG-based shape sensing has not been used as much as the other approaches, it is now a promising technology, especially after the advent of multi-core optical fibers (MCFs) [31], [32], which eliminates the issues arising from size and positioning problems of the single-core optical fibers. In addition, the advantages of FBG-based shape sensing include the absence of line of sight issues, being small in size, immunity to electromagnetic interference, flexibility, non-toxicity, and suitability for dynamic real-time applications.

In this study, FBG-inscribed MCFs have been used for feedback. To the best of the authors' knowledge, this is the first study investigating path-following control methods of steerable needles employing MCFs with FBGs. Also, this is the first experimental 3-D path-following study of PBNs.

This paper is organized as follows. The kinematic modeling of PBNs is presented in Section II. In Section III, the proposed control methods are introduced. In Section IV, the proposed shape reconstruction approach is outlined. This section is followed by Section V, where a simulation study and parameter tuning are explained. In Section VI, the experimental setup and experimental methods are described. Then, results are presented and discussed in Section VII, and lastly, the conclusion and future work are presented in Section VIII. The symbols and abbreviations used in these sections are summarized in Table I.

II. 3-D KINEMATIC MODELING OF PBNs

One of the most common methods used to model nonholonomic systems, such as steerable needles, is the parallel transport frame (PTF) [17], [33], which is used also in this study and satisfies the following frame equations.

$$\frac{d\boldsymbol{\gamma}(s)}{ds} = \boldsymbol{T}(s), \quad \frac{d\boldsymbol{T}(s)}{ds} = \kappa_1(s)\boldsymbol{N}_1(s) + \kappa_2(s)\boldsymbol{N}_2(s)$$

$$\frac{d\boldsymbol{N}_1(s)}{ds} = -\kappa_1(s)\boldsymbol{T}(s), \quad \frac{d\boldsymbol{N}_2(s)}{ds} = -\kappa_2(s)\boldsymbol{T}(s) \quad (1)$$

where $\boldsymbol{T}(s)$ is the unit tangent vector, and $\boldsymbol{N}_1(s)$, $\boldsymbol{N}_2(s)$ are the unit normal vectors. $\kappa_1(s)$ and $\kappa_2(s)$ describe the change of $\boldsymbol{T}(s)$ in the $\boldsymbol{N}_1(s)$ and $\boldsymbol{N}_2(s)$ directions at arc length position s and are calculated as follows:

$$\kappa_1(s) = \kappa(s)cos(\beta(s)), \quad \kappa_2(s) = \kappa(s)sin(\beta(s)) \quad (2)$$

where $\kappa(s)$ and $\beta(s)$ are the curvature value and the bending angle, respectively. The PBN tip reference frame and the curvature pair are illustrated in Fig. 2

One of the main advantages of the PTF over one of the other commonly used techniques, the Frenet-Serret frame, is that the PTF is defined for every curve $\boldsymbol{\gamma} \in \mathbf{SE3}$ including zero curvature while the Frenet-Serret frame requires a nonzero curvature to be defined.

PBNs can steer in full 3-D space, and readers may refer to [12] and [17] for further information regarding reachable curvatures. Because of the mechanical properties of PBNs, the relationship between the relative offsets of PBN segments and $\kappa(s)$ is not the same in all bending directions. This characteristic has been addressed for 4-segment PBNs by several studies in the literature, such as [12], and [17]. Because of its advantages for simple implementation, the latter has been adapted in this study, and is given as follows:

$$\dot{\boldsymbol{c}}_t = b\eta\boldsymbol{I}\,\boldsymbol{\Pi}\,\dot{\boldsymbol{o}}_t + \dot{\boldsymbol{\omega}}_t \quad (3)$$

TABLE I
NOMENCLATURE

α_1, α_2	ADRC parameters to be optimized
$\beta(s)$	Bending direction at arc length position s
$\beta_{1,2}^L, \beta_{1,2}^N$	ADRC parameters to be optimized
$\boldsymbol{\gamma}(s), \boldsymbol{\gamma}_{gt}(s), \boldsymbol{\gamma}_{tip}$	Curve points, reference path, and reconstructed tip position
δ	An ADRC parameter to be optimized
$\varepsilon, \varepsilon_0$	Strain and strain bias
$\boldsymbol{\zeta}_1, \boldsymbol{\zeta}_2$	Estimation of system states and the extended state
η	A PBN model parameter
θ_i	Bending direction of the ith PBN segment
θ_{12}, θ_{13}	Angles shown in Fig. 6
κ_1, κ_2	Curvature pair components
κ, κ_{max}	Curvature and the maximum curvature along $\boldsymbol{\gamma}_{gt}$
λ, λ_B	Wavelength and Bragg wavelength
Λ	FBG grating period
ν_s, ν_{all}	Speed for single PBN segment and all the segments
$\boldsymbol{\Pi}$	A matrix as defined in (4)
ω_o	ESO bandwidth
$\boldsymbol{\omega}$	Nonlinear function representing general disturbance
$\boldsymbol{A}$	Twist matrix
ADRC	Active Disturbance Rejection Control
b, b_0	Control gain and its estimation
$\boldsymbol{c}, \boldsymbol{c}^d$	Curvature pair and desired curvature pair
d	The radius of the circle shown in Fig. 6
D, D^d	Diagonal segment and desired diagonal segment.
DTG	Draw Tower Grating
$\boldsymbol{e}, \boldsymbol{e}_\kappa$	LLC error and ESO error
ESO	Extended State Observer
FBG	Fiber Bragg Grating
h	ADRC sampling period
HLC	High-level controller
$\boldsymbol{I}$	2×2 identity matrix
$\boldsymbol{J}$	Cost function to generate PBN offsets
k_p	The proportional controller gain
L, L^d	Leading segment and desired leading segment
L_f, L_r	Fiber length and reference-path length
LADRC	Linear ADRC
LLC	Low-level controller
m	Navigation length after PBN tip programming
MCF	Multi-core fiber
n	Number of intersection points of $\boldsymbol{\gamma}_{gt}$ and NLGL's sphere
n_{eff}	Effective refractive index
$\boldsymbol{N}_1, \boldsymbol{N}_2$	Parallel Transport Frame lateral axes
NLGL	Nonlinear Guidance Law
NADRC	Nonlinear ADRC
$o_i, \boldsymbol{o}^d, o_{max}$	i^{th} PBN segment's offset, desired PBN segment offsets, and the maximum allowed offset
p_e	photo-elastic coefficient
$\boldsymbol{p}_s, \boldsymbol{p}_T$	NLGL's pseudo-target point and PBN tip position
PBN	Programmable bevel-tip steerable needle
PTF	Parallel transport frame
$\boldsymbol{Q}$	Weight matrix for SQP
r	The radius of NLGL's virtual sphere
s	Arc length parameter
S_1, S_2	Two PBN segments other than L and D
SQP	Sequential Quadratic Programming
t	Subscript denoting discrete time step
$\boldsymbol{T}$	Parallel Transport Frame's tangent vector
$\boldsymbol{u}, \boldsymbol{u}_0$	Controller outputs as shown in Fig. 5
$\boldsymbol{X}, \boldsymbol{X}^d$	Pose matrix and desired pose matrix

where subscript t denotes the discrete time step, b is the control gain, which is unity in our system, $\boldsymbol{c}_t = \begin{bmatrix} \kappa_{1,t} & \kappa_{2,t} \end{bmatrix}^T \in \mathbb{R}^{2\times1}$ is the

estimated potential curvature pair at PBN tip (Fig. 2), $\eta \in \mathbb{R}$ is a constant optimized experimentally, $\boldsymbol{I}$ is a 2×2 identity matrix, $\boldsymbol{o}_t = \begin{bmatrix} o_{1,t} & o_{2,t} & o_{3,t} & o_{4,t} \end{bmatrix}^T \in \mathbb{R}^{4\times1}$ denotes the relative offsets of PBN segments which are with respect to the backmost segment (i.e., the closest to the proximal end - Fig. 2), $\boldsymbol{\omega}_t \in \mathbb{R}^{2\times1}$ is a nonlinear function representing general disturbance, and finally $\boldsymbol{\Pi} \in \mathbb{R}^{2\times4}$ is given as:

$$\boldsymbol{\Pi} = \begin{bmatrix} cos(\theta_1) & cos(\theta_2) & cos(\theta_3) & cos(\theta_4) \\ sin(\theta_1) & sin(\theta_2) & sin(\theta_3) & sin(\theta_4) \end{bmatrix} \quad (4)$$

where $\theta_1 = \frac{\pi}{4} \pm \pi$, $\theta_2 = \frac{3\pi}{4} \pm \pi$, $\theta_3 = \frac{5\pi}{4} \pm \pi$, $\theta_4 = \frac{7\pi}{4} \pm \pi$ denoting the bending directions of the PBN segments.

In [17], it is stated that the general relationship between the relative segment offsets and the projected curvature in the orthogonal axes, which led to (3), was derived from experimental data by assuming that the model was linear and could be represented by the first order approximation of the Taylor's expansion.

III. PATH-FOLLOWING CONTROLLER

The purpose of the controller is to generate a PBN tip configuration that guides the needle throughout a predefined path, given the PBN-tip curvature pair and tip pose. The overall controller consists of two parts; a high-level controller (HLC) and a low-level controller (LLC). The HLC generates desired curvature pairs, $\boldsymbol{c}_t^d = \begin{bmatrix} \kappa_{1,t}^d, \kappa_{2,t}^d \end{bmatrix}^T$, defined in PBN tip frame, for the LLC, which then tracks them by manipulating the individual segments. The block diagram of the overall controller is given in Fig. 3.

A. High-level controller

In this study, we implemented a nonlinear guidance law [29], [30] (NLGL)-based path-following controller. This method is based on defining a pseudo-target point, $\boldsymbol{p}_{s,t} \in \mathbb{R}^{3\times1}$, on the reference path, $\boldsymbol{\gamma}_{gt}(s) \in \mathbb{R}^{3\times1}$, at each time step, and estimating the desired curvature values for guidance. In [29] and [30], the NLGL was implemented to control unmanned aerial vehicles. $s \in [0, L_r]$ is the arc-length parameter for the reference path with L_r being the reference-path length. To define $\boldsymbol{p}_{s,t}$, a virtual sphere of radius r centered at the PBN tip is defined, as shown in Fig. 4. Then, the further forward one of the two sphere - reference path intersection points, of which number is denoted by $n \in \mathbb{N}_{\leq2}$, along the path is defined as $\boldsymbol{p}_{s,t}$, which, thus, guarantees smooth convergence. In the case where there is no intersection between the sphere and the reference path (i.e., $n = 0$), $\boldsymbol{p}_{s,t}$ is defined as the point on the desired path closest to the sphere. This is followed by the calculation of the desired curvature pair, $\boldsymbol{c}_t^d$ as given in Algorithm 1. To ensure $n \in \mathbb{N}_{\leq2}$, r is defined as $r < 1/\kappa_{max}$, with κ_{max} being
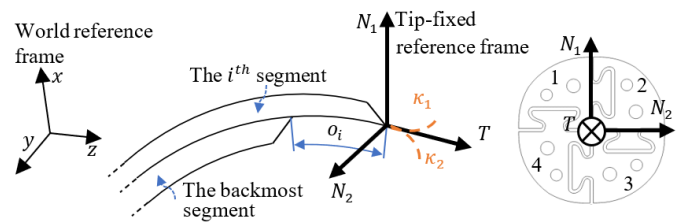

Fig. 2. An illustration of the world reference frame, the PBN tip-fixed frame, which is fixed at the tip of the leading segment, and the curvature pair. Left: The PBN is illustrated in 2-D for clarity. $\boldsymbol{o}_i$ represents the relative offset of the ith PBN segment with $i \in \{1, 2, 3, 4\}$ (The relative offset of the backmost segment, the closest to the proximal end, is 0). Right: Cross-section view of a PBN with the frame at the tip. The segment numbers are shown on the segments

the maximum curvature along the reference path. In [29], it was demonstrated that the NLGL is asymptotically-stable in the entire state space of useful initial conditions, which guarantees that the path-following error converges to zero. In the case of tissue motion, the path-following error is expected to converge to zero from the new initial conditions.

Algorithm 1 HLC algorithm - all the positions and axes are defined with respect to the world reference frame.

Input: Reference Path: $\boldsymbol{\gamma}_{gt}(s)$, The radius of the virtual sphere: r, Needle tip position: $\boldsymbol{p}_{T,t} \in \mathbb{R}^{3\times1}$, Needle tip frame axes: $\boldsymbol{T}_t, \boldsymbol{N}_{1,t}, \boldsymbol{N}_{2,t} \in \mathbb{R}^{3\times1}$, Navigation length: m (set manually)

   Output: The desired curvature pair: $\boldsymbol{c}_t^d$

1: $n \leftarrow$ Number of intersection points of the sphere and the reference path
2: **if** $n = 2$ **then**
3:     $\boldsymbol{p}_{s,t} \leftarrow$ The further forward intersection point along the reference path
4: **else if** $n = 1$ **then**
5:     **if** $\left\| \boldsymbol{p}_{T,t} - \boldsymbol{\gamma}_{gt}(0) \right\| < \left\| \boldsymbol{p}_{T,t} - \boldsymbol{\gamma}_{gt}(L_r) \right\|$ **then**
6:       $\boldsymbol{p}_{s,t} \leftarrow$ The single intersection point
7:     **else**
8:       $\boldsymbol{p}_{s,t} \leftarrow \boldsymbol{\gamma}_{gt}(L_r)$
9:     **end if**
10: **else if** $n = 0$ **then**
11:     $\boldsymbol{p}_{s,t} \leftarrow$ The reference path point closest to the sphere
12: **end if**
13: $\boldsymbol{T}_t^d = (\boldsymbol{p}_{s,t} - \boldsymbol{p}_{T,t}) / \left\| \boldsymbol{p}_{s,t} - \boldsymbol{p}_{T,t} \right\|$
14: $\boldsymbol{N}_{1,t}^d = (\boldsymbol{N}_{2,t} \times \boldsymbol{T}_t^d) / \left\| \boldsymbol{N}_{2,t} \times \boldsymbol{T}_t^d \right\|$
15: $\boldsymbol{N}_{2,t}^d = (\boldsymbol{T}_t^d \times \boldsymbol{N}_{1,t}^d) / \left\| \boldsymbol{T}_t^d \times \boldsymbol{N}_{1,t}^d \right\|$
16: $\boldsymbol{X}_t = \begin{bmatrix} \boldsymbol{T}_t & \boldsymbol{N}_{1,t} & \boldsymbol{N}_{2,t} & \boldsymbol{p}_{T,t} \\ 0 & 0 & 0 & 1 \end{bmatrix}$ {Pose matrix}
17: $\boldsymbol{X}_t^d = \begin{bmatrix} \boldsymbol{T}_t^d & \boldsymbol{N}_{1,t}^d & \boldsymbol{N}_{2,t}^d & \boldsymbol{p}_{s,t} \\ 0 & 0 & 0 & 1 \end{bmatrix}$ {Desired pose matrix}
18: $\boldsymbol{A}_t = \ln(\boldsymbol{X}_t^{-1} \boldsymbol{X}_t^d)/m$ {Twist matrix [32]}
19: $\boldsymbol{c}_t^d = \begin{bmatrix} 0 & 1 & 0 & 0 \\ 0 & 0 & 1 & 0 \end{bmatrix} \boldsymbol{A}_t \begin{bmatrix} 1 & 0 & 0 & 0 \end{bmatrix}^T$

B. Low-level controller

In this section the process from the generation of the desired curvature pair, $\boldsymbol{c}_t^d$, to the completion of PBN tip programming, and the movement of the PBN with the programmed tip is given in three subsections: (i) ADRC to generate curvature control inputs, (ii) Sequential Quadratic Programming (SQP) to generate PBN segment offsets, (iii) PBN tip programming. The block diagram of the LLC is given in Fig. 5.
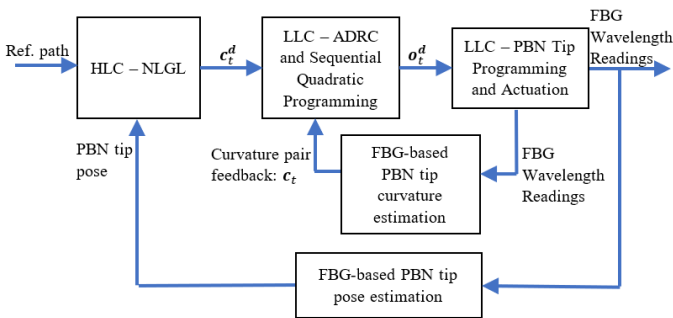
Fig. 3. Overall path-following controller and data processing diagram
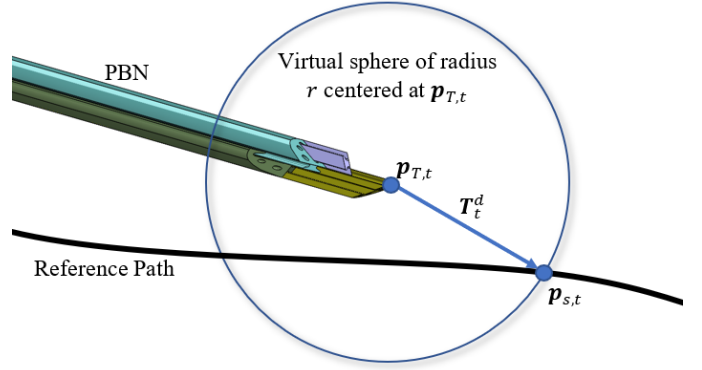
Fig. 4. Illustration of the NLGL

1) ADRC to generate curvature control inputs:
The ADRC is used to track the desired curvature pair, $\boldsymbol{c}_t^d$, generated by the HLC. The subscript t is omitted in this section for clarity, and all the variables are defined for time step t unless indicated otherwise.

Rewriting the model of our multi-input and multi-output (MIMO) system (3) in a more compact form:

$$\dot{\boldsymbol{c}} = b\,\boldsymbol{u} + \dot{\boldsymbol{\omega}} \tag{5}$$

where $\boldsymbol{u} = \eta \boldsymbol{I} \boldsymbol{\Pi} \dot{\boldsymbol{o}}$, and b is the control gain, which is unity in our system.

Both a linear ESO, which is similar to Luenberger observer [34], and a nonlinear ESO have been designed to estimate the system state $\boldsymbol{c}$ and the total disturbance (i.e., the extended state), which are tracked with $\boldsymbol{\zeta}_1 \in \mathbb{R}^{2\times1}$ and $\boldsymbol{\zeta}_2 \in \mathbb{R}^{2\times1}$, respectively.

$$\boldsymbol{\zeta}_1 \approx \boldsymbol{c}, \qquad \boldsymbol{\zeta}_2 \approx (b - b_0)\boldsymbol{u} + \dot{\boldsymbol{\omega}} \tag{6}$$

with b_0 being the estimation of the control gain b. $\boldsymbol{\zeta}_1$ is the estimation of the curvature pair, $\boldsymbol{c}$, and $\boldsymbol{\zeta}_2$ is the estimations of the total disturbance, which is the combination of the disturbance caused by the control gain's estimation error and the derivative of disturbance, $\dot{\boldsymbol{\omega}}$, as defined in (3). The potential factors causing disturbance could include the heterogeneity of the tissue in which the PBN is inserted, nonuniform friction between PBN segments, tissue displacements during needle navigation, and the tendon-driven effect caused by the wires of proprioceptive sensors placed away from the neutral axis of the PBN segments. The elimination of these uncertainties are the main motivation of using a closed-loop controller and are actively compensated for by the ADRC in this study. The stability analysis for the LADRC is given in Appendix, and readers may refer to [35] for the stability analysis of the NADRC.

The ADRC parameters are not directly dependent on the tissue type and the plant's mathematical model. Rather, they are functions of how fast the plant changes [25].

The control law is given as:

$$\boldsymbol{u} = \frac{\boldsymbol{u}_0 - \boldsymbol{\zeta}_2}{b_0} \tag{7}$$
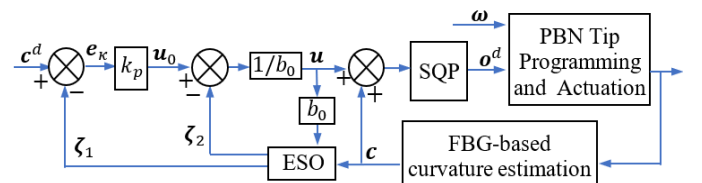
Fig. 5. Overall LLC block diagram (subscript t is omitted for clarity)

Therefore, disturbances are assumed to be eliminated provided that they vary slowly, and (5) can be simplified as $\dot{c} \approx u_0$ where the controller output $u_0 \in \mathbb{R}^{2 \times 1}$ is defined as follows:

$$u_0 = k_p \, e_\kappa \qquad (8)$$

where k_p is the proportional controller gain, and $e_\kappa = c^d - \zeta_1$ denotes the error of the states.

The linear ESO is given in discrete form as follows [26]:

$$\begin{cases} e = c - \zeta_1 \\ \zeta_{1,t+1} = \zeta_1 + h(\zeta_2 + b_0 u + \beta_1^L e) \\ \zeta_{2,t+1} = \zeta_2 + h\beta_2^L e \end{cases} \qquad (9)$$

where h is the sampling period. β_1^L and β_2^L are given as $3\omega_0$ and $3\omega_0^2$, where ω_0 is the observer bandwidth [36].

Similarly, the discrete nonlinear ESO is given as follows:

$$\begin{cases} e = c - \zeta_1 \\ \zeta_{1,t+1} = \zeta_1 + h(\zeta_2 + b_0 u + \beta_1^N fal(e, \alpha_1, \delta)) \\ \zeta_{2,t+1} = \zeta_2 + \beta_2^N fal(e, \alpha_2, \delta) \end{cases} \qquad (10)$$

where β_1^N is a constant to be optimized, and β_2^N is a function of h and given as $\beta_2^N = 2/(5^2 h^{1.2})$. Finally, $fal(.)$ is a nonlinear function as follows:

$$fal(e, \alpha, \delta) = \begin{cases} e/(\delta^{1-\alpha}), & |e| \leq \delta \\ |e|^\alpha sign(e), & |e| > \delta \end{cases} \qquad (11)$$

where $\alpha \in \mathbb{R}_{<1}$ is a parameter to be optimized experimentally with δ. Readers may refer to [25] and [36], which include ESO equations for single-input-single-output systems, for more information about definitions of ADRC parameters.

2) Sequential Quadratic Programming to generate PBN segment offsets: The incremental curvature commands, u are added with feedback curvature values, c, and mapped into the desired relative offsets of the PBN segments, o^d, via SQP technique, which was originally proposed in [19], and summarized here for completeness:

$$min \; \mathrm{J} = \frac{1}{2} o^T Q o \qquad (12)$$

with constraints

$$\begin{cases} u + c = \eta I \, \Pi \, o_t \\ o_i \leq o_{max} \end{cases} \qquad (13)$$

where Q is the weight matrix of the PBN segments, and o_{max} is the maximum allowed relative distal offset according to the physical limitations of the PBN (i.e, the limitation to eliminate the risk of separation of segments).

3) PBN tip programming: In the last step, an actuation unit drives the PBN segments to program the PBN tip according to the desired segment offsets, o^d, as given in Algorithm 2, which is explained in this section.

At the end of the programming, it is desired to have the same PBN tip position as in the beginning. Besides, the PBN tip should be kept fixed even during the programming to eliminate re-insertion and to decrease tissue damage. To this end: (i) If the leading segment should remain unchanged (the segment with the highest o^d is the same as the current leading one), it is kept fixed while others move to meet o^d, (ii) otherwise, the desired leading segment, L^d, is driven next to the current leading segment, L, and the segments other than L^d are arranged such that the resulting relative offsets satisfy o^d. L is not pulled back before L^d is driven next to it with or without one of the other two segments (in the case of our 4-segment PBN). The reason why another segment might be required to be driven next to L is to

satisfy the permissibility conditions of PBNs [12], e.g., two diagonal segments not to be driven forward (together or individually) in the case when they are ahead of the other two.

The desired insertion lengths of the PBN segments, which are some of the inputs of Algorithm 2, are calculated using the current insertion lengths and o^d by considering the discrepancy between the distal and the proximal offsets, which is expected to occur when the PBN follows a curvilinear path. To account for this, the method proposed in [12] (Section V.C) is used and the details are not given in this study.

Also taking into account the limitations of the actuation unit, the segment speeds are empirically set to ν_s, which was found to be appropriate to minimize tissue damage and operation time.

Finally, when the programming is completed, all the segments are pushed forward with the speed of ν_{all} for a distance of m to realize the desired curvature. The speed, ν_{all}, is selected to be less than ν_s given that the tissue damage is expected to be higher when all the segments are driven into the tissue at the same time [37].

Algorithm 2 The PBN tip programming algorithm for a 4-segment PBN satisfying the permissibility conditions [12] - The commands at each step are performed simultaneously.

Input: Current leading segment: L, desired leading segment: L^d, the segment located at the diagonal of L (not one of the neighboring segments): D, the segment located at the diagonal of L^d: D^d, The desired insertion lengths of the PBN segments.

1: $S_1, S_2 \leftarrow$ The segments other than L and D
2: **if** $L^d = L$ **then**
3:     **if** D is desired to move backward **then**
4:         Retract D to the desired length,
         Position S_1 and S_2 to the desired length that the one to be back moves after the other one finishes
5:     **else**
6:         Position S_1 and S_2 to the desired length that the one to be back moves after the other one finishes
7:         Drive D to the desired length
8:     **end if**
9: **else if** $L^d = D$ **then**
10:     $S_a \leftarrow$ The further extended one of S_1 and S_2
11:     $S_b \leftarrow$ The hind one of S_1 and S_2
12:     Drive S_a forward till the tip of L,
     Drive L^d forward till the tip of S_a
13:     Retract L to the desired length,
     Position S_b to the desired length,
     Retract S_a to the desired length
14: **else**
15:     Drive L^d to the desired length
16:     Position D to the desired length,
     Position D^d to the desired length
17:     Retract L to the desired length
18: **end if**

IV. PBN Tip Pose Reconstruction and curvature estimation with FBG-inscribed Optical Fibers

FBG-based curvature estimation and shape reconstruction methods are summarized in this section. A detailed explanation, including 3-D validation, of these methods are given in [31], where the mean and maximum PBN tip absolute position errors, and the standard deviation are found with a 120-mm insertion to be 2.87 mm, 5.76 mm, and 1.63 mm, respectively. The assumptions mentioned in this section are not discussed in this study. Readers may refer to [31] for the details.

1) FBG Theory and Curvature Estimation: An FBG is a grating with a period Λ, etched onto optical fibers, and has the property of reflecting the light of a specific wavelength, Bragg wavelength:

$$\lambda_B = 2n_{eff}\Lambda \tag{14}$$

where n_{eff} is the effective refractive index. The reflected wavelength shift is a function of strain and temperature:

$$\Delta\lambda = \lambda_B((1 - p_e)\varepsilon + (\alpha_\lambda + \alpha_n)\Delta T) \tag{15}$$

where p_e is the photo-elastic coefficient, α_λ is the thermal expansion coefficient, and α_n is the thermo-optic coefficient [38]. When $\Delta T = 0$, the strain is given as follows (In this study, the temperature change is accounted for with the method given in the next paragraph):

$$\varepsilon = \frac{\Delta\lambda}{\lambda_B(1 - p_e)} \tag{16}$$

The axial strain values that FBGs at off-centered cores of the fibres experience can also be calculated from mechanics principles. Assuming that the fiber behaves as a symmetric, uniform rod, and is in pure bending and of circular cross section, the strain values corresponding to the 3 off-centered cores are given as follows:

$$
\begin{aligned}
\varepsilon_1(s) &= -\kappa(s)\delta_1(s) = -\kappa(s)d\,cos(\beta(s)) + \varepsilon_0(s) \\
\varepsilon_2(s) &= -\kappa(s)\delta_2(s) = -\kappa(s)d\,cos(\beta(s) + \theta_{12}) + \varepsilon_0(s) \\
\varepsilon_3(s) &= -\kappa(s)\delta_3(s) = -\kappa(s)d\,cos(\beta(s) + \theta_{13}) + \varepsilon_0(s)
\end{aligned}
\tag{17}
$$

where the arc length parameter s is defined in $(0, L_f)$, with L_f being the length of the fiber. $\delta_j(s)$ is the distance between the fiber's neutral bending plane and the center of the jth core, with $j \in \{1, 2, 3\}$. d is the radius of the circle made up by the cores at the fiber cross-sections. The bending direction, $\beta(s)$, is with respect to the 1st core. θ_{12} and θ_{13} are the angular offsets from the 1st core to the 2nd and the 3rd cores, respectively. $\varepsilon_0(s)$ is the strain bias. It is assumed that the temperature change equally affects the gratings of each FBG set due to the proximity of the MCF cores, which enables the temperature change to reflect on $\varepsilon_0(s)$ and thus, be taken into account. An example configuration to illustrate these parameters is given in Fig. 6. Therefore, this equation set is solved for $\kappa(s), \beta(s)$, and $\varepsilon_0(s)$. Although the explanation is given for 3 off-centered cores for brevity, in the presence of more than 3 off-centered cores, as in the validation experiments in this study, the equations from redundant cores are used to increase accuracy [31].
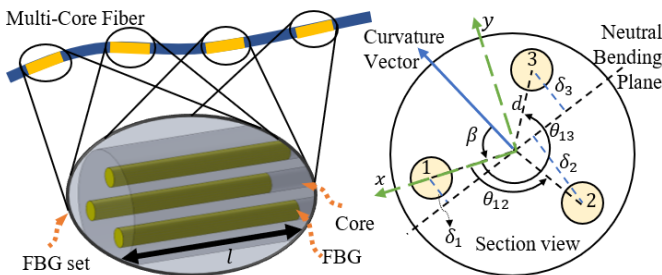

Fig. 6. Left: FBG-inscribed MCF including 3 off-centered cores. l denotes the FBG length. Right: Cross-section of an MCF. The cores are denoted by the numbers: $1, 2, 3$. d is the radius of the circle made up by the core centers. δ_j is the distance between the neutral bending axis and the jth core center, with $j \in \{1, 2, 3\}$. The local frame fixed to the cross-section is denoted by the x, y axes. β is the angular offset from the curvature vector to the 1st core. θ_{12} is the angle from the 1st core to the 2nd core. Similarly, θ_{13} is the angle from the 1st core to the 3rd core.

2) FBG-based Tip Pose Reconstruction: The nature of the FBG-based tip pose reconstruction, which utilizes curvature vectors from the needle's base to tip, requires the reconstruction of the entire needle. We propose averaging the individual fibers' curvature vectors to reconstruct the PBN. Eventually, the shape is reconstructed by integrating the tangent vectors, $\boldsymbol{T}(s)$, which are calculated from the averaged curvature vectors using the method given in equations (1) and (2). All the curves created by the MCFs and the PBN are assumed to be a regular unit-speed space curve in $\mathbb{R}^3$. Also, the MCFs are assumed to be in pure bending, and they are modeled as symmetric rods (circular cross-section) with uniform-density. The torsion that the PBN is exposed to is assumed to be negligible, as helically-wrapped fibers are required to distinguish between torsion and bending [39] (This assumption is for sensing only, and it is not required for the controller proposed in this study).

The FBG locations on the MCFs are known *a priori*. Several interpolation methods to estimate the curvature vectors in between the finite number of FBGs along an MCF have been proposed [40]. However, we propose using the curvature vectors created by the FBG at the MCF tip along the insertion, which eliminates the need for an interpolation method thanks to the frequent curvature vector acquisitions over the navigation length. This method exploits the follow-the-leader nature of steerable needles, i.e., at any discrete time step of a soft-tissue insertion, the curvature vectors created by the tip FBG during the previous time steps are equivalent to the ones covering the MCF length from tissue entry to tip. The discrete curve points, to which the curvature vectors correspond, along the path are assumed to be fixed to the tissue. New points are created as the fiber tip continues to advance. When the FBGs other than the tip FBG enter the tissue and start recording curvatures, previously acquired curvature vectors by the tip FBG are fused with newly acquired ones via a Kalman filter. Therefore, shape sensing accuracy is increased and possible soft tissue movements along the needle length are addressed. The potential errors that would result from interpolation methods are also eliminated. This method allows the shape reconstruction of steerable needles that are longer than the sensorized length of their MCFs without the need for extrapolation. In the case where there is an unsensorized length between the tip FBG set and the segment tip, the curvature vector obtained by the tip FBG set are assigned to this length ("lead-out" length) as well.

V. SIMULATIONS AND PARAMETER OPTIMIZATION

The developed control methods were initially tested with a series of simulations, by means of which the controller parameters were optimized with the interior point algorithm [41] in MATLAB. The methods given in Section II were used to model the needle steering. Eight point-wise virtual FBG sets with 14 mm separation were modeled, and white Gaussian noise was added to the calculated curvature values to imitate the FBG measurement noise. The FBG measurement noise covariance matrix proposed in [31] was used to generate the FBG noise. An error measure, the absolute difference between the PBN tip position and the ground truth, was defined to quantify the performance, as follows:

$$e_{pos} = \left\| \boldsymbol{\gamma}_{tip} - \boldsymbol{\gamma}_{gt}(s) \right\| \tag{18}$$

where $\boldsymbol{\gamma}_{tip}$ is the reconstructed PBN tip position, and $\boldsymbol{\gamma}_{gt}(s)$ is the ground truth of the tip position. The 3-D reference path used in the simulations consists of 3 parts, and it is given in Fig. 7 and Table II. The results of the simulations using linear ESO and nonlinear ESO are given in Fig. 7, Fig. 8, and Table III, which were conducted using the finalized controller parameters given in Table IV. When optimizing the parameters, the step navigation length, m,

	Length [mm]	Curvature [1/m]	Bending Plane Orientation [°]
Section 1	10	Constant: 0	0
Section 2	55	Constant: 6.67	15
Section 3	55	Constant: 5	105

	$\bar{e}_{pos}$	$\sigma_{e_{pos}}$	$e_{pos,max}$	$e_{pos,target}$
NLGL - LADRC:	0.17	0.11	0.42	0.16
NLGL - NADRC:	0.26	0.13	0.54	0.32

was constrained with $m \geq 5$ mm to achieve a reasonable insertion duration. In the simulations, the initial position of the PBN was 1.5 mm off-path in both x and y directions.

With regards to the simulation results (Fig. 7, Fig. 8, Table III), no recognizable difference was seen between the performances of the controllers with linear and nonlinear ESO. The convergence to the path, in both cases, was achieved after approximately 20 mm navigation, and the error stayed below 0.5 mm along the rest of the path.

Finally, compared to the sliding-mode PBN controller presented in [19], the settling time was lowered in this study by keeping the steady-state error in the acceptable margin.

VI. EXPERIMENTAL EVALUATION

In this section, the experimental setup and details about the experimental methods are provided. In addition to the path-following experiments, we also conducted target-hitting experiments, where
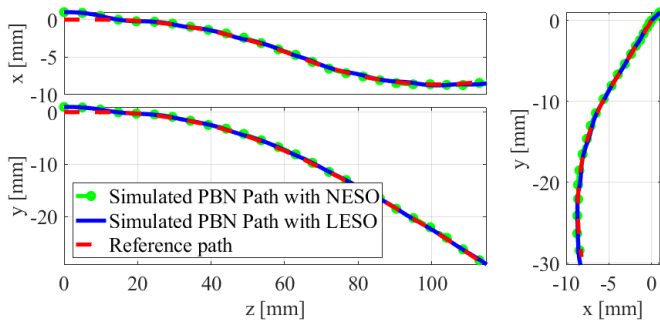

Fig. 7. Path planning simulation results with initial perturbation of 1 mm in x and y directions, and illustration of the 120-mm 3-D path used in the simulations and experiments
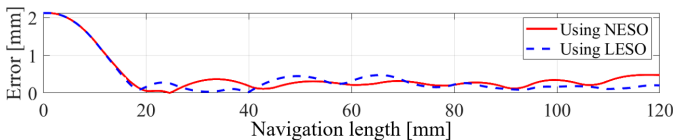

Fig. 8. Absolute position error, e_{pos}, of simulated PBN paths with initial perturbation of 1.5 mm in x and y directions

NLGL - LADRC						
r	k_p	$\boldsymbol{Q}$	h	o_{max}	ω_o	m
5 mm	2.48	$\boldsymbol{I}$	0.076 s	30 mm	1.32	5 mm

NLGL - NADRC					
r	k_p	$\boldsymbol{Q}$	h	α_1	α_2
4 mm	3.4	$\boldsymbol{I}$	0.11 s	0.7	0.45

δ	m	β_1^N	o_{max}
0.56	5 mm	1.74	30 mm

the virtual target moves, to assess the proposed control method's performance in the case where target migration occurs as a result of tissue movement.

In total, 6 *ex vivo* and 12 *in vitro* path-following, and 6 *in vitro* target-hitting experiments were conducted. The *ex vivo* tests were performed in sheep brains that were placed in a tissue phantom, as seen in Fig. 9. The *ex vivo* tissue was purchased from a local butcher, and several of the brains were used to create enough volume for steering. On the other hand, a gelatin phantom produced from 7% by weight bovine gelatin, an approximation for human brain [42], was used as a soft-tissue stimulant for the *in vitro* tests.

The navigation speeds, ν_{all} and ν_s, were selected as 1 mm/s and 5.5 mm/s respectively, as recommended in [18] for neurosurgery. All the parameters used in the experiments are given in Table V.

The experiments were considered completed when the distance between the target and the plane that is orthogonal to the tip-fixed axis $\boldsymbol{T}$ became 0. The following subsections explain the setup and the experiments, which are summarized in Table VI. Although similar performances were obtained from the simulations with LADRC and NADRC, both controllers were also assessed experimentally to aid a more realistic comparison.

A. Setup

In the experiments, a clinically-sized (2.5 mm in diameter), medical-grade 4-segment PBN instrumented with 4 MCFs was used (Fig. 1). It was produced from a medical-grade polymer (plasticized polyvinyl chloride) with 86 Shore "A" hardness by Xograph Healthcare Ltd. (Gloucestershire, United Kingdom) via extrusion. Nano-coating with Poly(para-xylylene) was formed on the surface of the segments to reduce friction between them. Each PBN segment has 0.25 mm and 0.3 mm working channels; the latter is used to accommodate MCFs, which were fixed at the segment bases. Only 4 of the 6 off-centered cores of MCFs were used since the optical spectrum interrogator (FBGS International NV (Geel, Belgium) - FBG-scan 804D) used in this study had only four channels. The specifications of the fibers are given in Table VII. Regarding the MCF production method, Draw Tower Gratings (DTG®) were used. In this method, gratings are inscribed just before the fiber-coating process, and striping and re-coating as in standard FBG inscription techniques are not required, leading to the high strength of multi-core fibers. The FBGs used in this work had a 12 mm lead-out length, which is the length between the fiber tip and and the FBG set that is closest to the fiber tip.

The PBN segments were driven using an actuation unit consisting of 4 linear actuators. Each of these actuators included an EC20 Flat Motor (351007, Maxon Motor, Switzerland), which was connected to a 19:1 gearbox (GP22A, Maxon Motor, Switzerland) and a lead screw. The lead screw was attached to a PBN segment via an anti-backlash nut and a transmission link. The mechanical slack in the system was assumed to be negligible as in previous studies [12],

TABLE V
CONTROLLER PARAMETERS FOR EXPERIMENTS

	r	k_p	$\boldsymbol{Q}$	h	o_{max}	ω_o	m	η_s	η_{all}	α_1	α_2	δ	β_1^N
NLGL - LADRC	5 mm	0.5	$\boldsymbol{I}$	0.076 s	30 mm	1.32	5 mm	5.5 m/s	1 m/s	-	-	-	-
NLGL - NADRC	5 mm	0.7	$\boldsymbol{I}$	0.11 s	30 mm	-	5 mm	5.5 m/s	1 m/s	0.7	0.45	0.56	1.74

TABLE VI
THE SPECIFICATIONS OF TRIPLEX EXPERIMENT GROUPS

Triplex Encoding	Controller	Initial Perturbation	Tissue Type	Exp. Type
N_Pert_Ph_PF (Exp. 1-2-3)	NLGL & NADRC	x: 1.5 mm y: 1.5 mm	Phantom	Path Following
L_Pert_Ph_PF (Exp. 4-5-6)	NLGL & LADRC	x: 1.5 mm y: 1.5 mm	Phantom	Path Following
N_Ph_PF (Exp. 7-8-9)	NLGL & NADRC	-	Phantom	Path Following
L_Ph_PF (Exp. 10-11-12)	NLGL & LADRC	-	Phantom	Path Following
N_Ex_PF (Exp. 13-14-15)	NLGL & NADRC	-	*Ex vivo*	Path Following
L_Ex_PF (Exp. 16-17-18)	NLGL & LADRC	-	*Ex vivo*	Path Following
N_Ph_TH (Exp. 19-20-21)	NLGL & NADRC	-	Phantom	Target Hitting
L_Ph_TH (Exp. 22-23-24)	NLGL & LADRC	-	Phantom	Target Hitting

TABLE VII
MCF SPECIFICATIONS - FBGS INTERNATIONAL NV (GEEL, BELGIUM)

Production technique	Draw Tower Gratings (DTG®)
Operating temperature	-20°C to 200°C
Wavelength configurations of the 4 MCFs	MCF 1: 1513.0nm - 1529.8nm
	MCF 2: 1532.2nm - 1549.0nm
	MCF 3: 1551.4nm - 1568.2nm
	MCF 4: 1570.6nm - 1587.4nm
Consecutive FBG Bragg- wavelength difference	2.4nm
Gage Factor $(1 - p_e)$	0.737
Interrogator model	FBGS FBG-scan 804D
Fiber coating	ORMOCER®-T
FBG Refractive Index	3%
Number of cores	7 cores – 1 centered, 6 off-centered
Number of FBG sets	8
FBG length	5 mm
Consecutive FBG center to center distance	14 mm
Sensorized fiber length	103 mm
Radius of the circle made up by the off-centered cores (d)	37 μm

[43], [44]. The actuation unit also included encoders (HEDR-55L2-BP07, Broadcom Inc.), which were connected to the lead screw shaft and used to determine the actual navigation length of each segment. The software for actuation, shape sensing, and path following were developed in-house using MathWorks MATLAB 2019b. The sensing was performed with a sampling frequency of 50 Hz. No fixed refresh rate for calculating HLC's pseudo-target point was used, as the time required for each loop is a function of the time required for the tip programming (Algorithm 2). The overall experimental setup is shown in Fig. 9.

After each experiment, the PBN was removed and placed at a different entry point to prevent a new experiment from being effected by a previous experiment's track.

In order to make the tasks more complex, the initial pose in target-hitting experiments and the bending angles of the reference path in path-following experiments were not aligned with any of the 8 principal directions of the PBN (Fig. 10) in which steering can be achieved relatively simply by one or two segments moving forward of the others [43].

Since the only source of information about the needle tip pose is from the FBG-based sensing, it is assumed here to be the true measurement. Therefore, in the experiments, the desired paths and the target paths are fixed in space as opposed to being relative to the tissue.

B. Path-following Experiments

In the path-following experiments, the same 3-D path used in the simulations was used as the reference path, and the experiment scenarios are illustrated in Fig. 11. The path was sampled at each 50 μm, which guarantees that the pseudo-target point, $\boldsymbol{p}_{s,t}$, was determined with a maximum of 25 μm positional error. In 12 of the path-following experiments, the PBN was pushed along, and

tangent to the path whereas it was off-path in the others, to assess the performance of the controller for a range of operating conditions. In all the experiments, the PBN was inserted to a depth of 120 mm, longer than the MCF length possessing the FBGs, which is 103 mm.

C. Target-hitting experiments

The virtual target started to move from a point that was 110 mm away from the PBN's starting point, in an arbitrary direction and by an amount equal to one fifth of the PBN tip's movement in the z axis at each step. This corresponds to 22 mm navigation of the target in total. This value, for about 120 mm PBN navigation, is approximately in agreement with the target navigation distance used in [20], where target hitting experiments were conducted with a 0.86 mm-diameter bevel-tip needle, and the target was moved approximately 10 mm over a length of about 80 mm insertion. When considering the ratio between the target movement length and the needle navigation, the value we used in our experiments was slightly higher compared to [20], which was to account for the size difference between the needles.

It was assumed that there is no obstacle in the tissue. Also, since there is no path to follow, the location of the target was assigned to the NLGL's pseudo-target point, $\boldsymbol{p}_{s,t}$, at each time step. When the experiments started, the initial orientation of the PBN was set to be towards the target, and the targets were moved in the x-y plane. The initial orientation of the tip frame with respect to the world frame is shown in Fig. 10. The target's motion was independent of the tissue-needle interaction, and the controller used only the current position of the target at each time step.
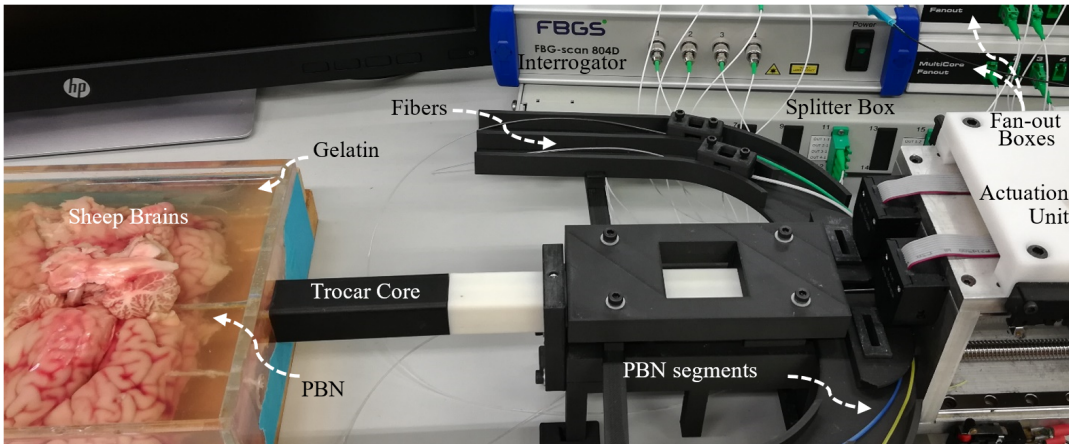
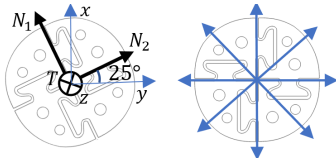Fig. 9. The overall *ex vivo* test setup

Fig. 10. Left: The initial orientation of the tip frame with respect to the world reference frame used in the target-hitting experiments. Right: 8 principal steering directions of PBNs.
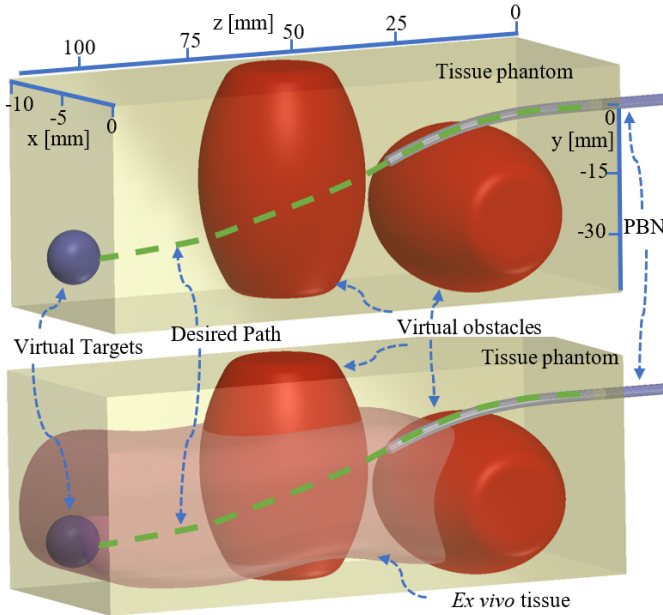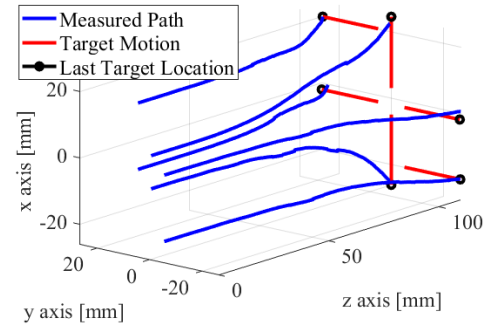

Fig. 12. The insertion paths and target motions from the 6 target-hitting experiments.
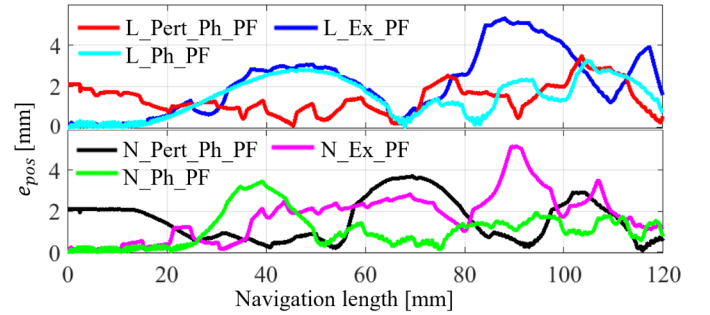

Fig. 13. The absolute position error results of one of the experiments from each triplex experiment group. The selected experiments are the ones for which the mean error is closest to that of their experiment group.

Fig. 11. Path-Following Experiments: *In vitro* (top) and *ex vivo* (bottom) - The virtual obstacles are included in this figure for illustration purposes, and they are not used in this study

VII. RESULTS AND DISCUSSION

The insertion paths and target motions from the six target-hitting experiments are presented in Fig. 12, showing that our algorithm guided the needle effectively towards the moving targets. The absolute position errors during the path-following experiments are shown in Fig. 13. It is seen that the controller manages to overcome the disturbances, including the ones caused by the transition from gelatin to tissue (at around 30 mm insertion length, for experiments 13 and 16). However, the maximum errors were obtained in *ex vivo* trials, as expected, because of the varying mechanical properties of the heterogeneous tissue. For illustration purposes, the individual segment movements during experiment 9 and 11, obtained from the encoders of the actuation unit, are shown in Fig. 14 and Fig. 15. These figures illustrate that the LLC effectively manipulated the individual segments to track the curvature commands from the HLC.

As shown, from time to time the difference between the minimum and maximum encoder values can reach 30 mm (the maximum allowable relative offset between segment tips), pushing the system to its limits (o_{max}). The desired curvatures generated by the HLC, alongside the estimated curvatures, are shown in Fig. 16 and Fig. 17. It is apparent that the tracking is achieved with a lag, which is mainly due to the lead-out length. Thus we expect that better results could be obtained with a shorter lead-out length.

The reference and measured trajectories are shown in Fig. 18 and Fig. 19, which show that the control law is able to track the reference path.

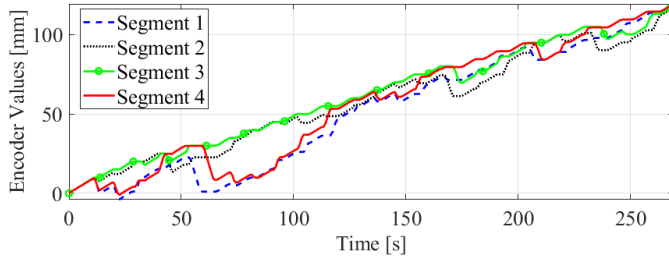Lastly, the experimental results are summarized in Table VIII. The

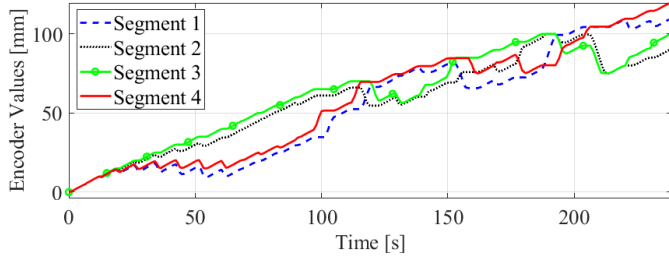Fig. 14. Movements of individual segments during experiment 9.

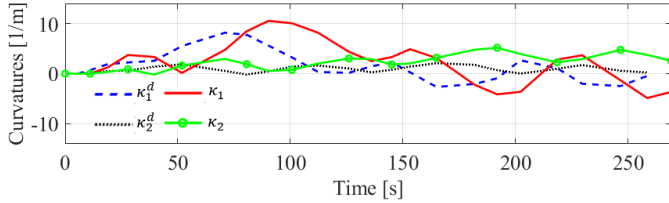Fig. 15. Movements of individual segments during experiment 11.

Fig. 16. Desired curvature pair (the output of the HLC) and estimated curvature pair for experiment 9.
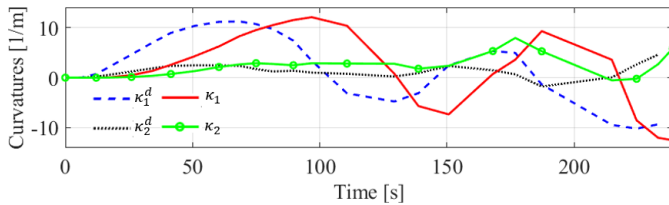

Fig. 17. Desired curvature pair (the output of the HLC) and estimated curvature pair for experiment 11.
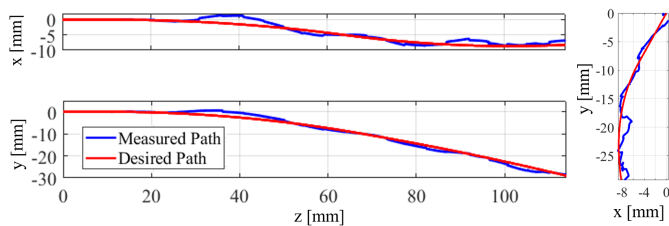

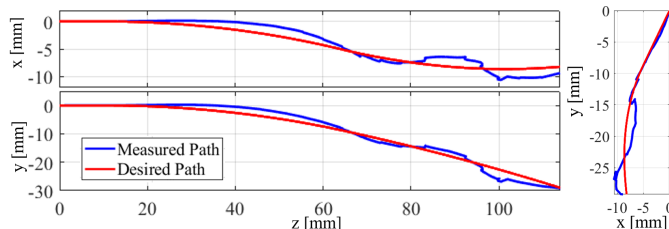Fig. 18. The reference path and the reconstructed path for experiment 9.

Fig. 19. The reference path and the reconstructed path for experiment 11.

TABLE VIII

EXPERIMENTAL RESULTS - ABSOLUTE POSITION ERROR [MM], e_{pos}, OVER 120 MM INSERTION LENGTH OF EACH TRIPLEX EXPERIMENT GROUP: MEAN: $\bar{e}_{pos}$, STANDARD DEVIATION: $\sigma_{e_{pos}}$, MAXIMUM: $e_{pos,max}$, MEAN TARGET ERROR : $\bar{e}_{pos,target}$.

	$\bar{e}_{pos}$	$\sigma_{e_{pos}}$	$e_{pos,max}$	$\bar{e}_{pos,target}$
N_Pert_Ph_PF	1.79	1.02	4.25	1.93
L_Pert_Ph_PF	1.6	0.72	3.87	2.49
N_Ph_PF	1.32	0.85	3.96	1.75
L_Ph_PF	1.70	0.93	3.61	2.62
N_Ex_PF	1.98	1.15	5.28	2.83
L_Ex_PF	2.37	1.54	5.84	2.91
N_Ph_TH	-	-	6.56	3.12
L_Ph_TH	-	-	5.28	2.5
Average	1.79	1.04	4.83	2.52

results of target-hitting experiments (Exp N_Ph_TH and L_Ph_TH) were calculated with the last PBN tip position data. Without considering the error of the shape sensing method used in this study, the mean tracking error for sheep brain is 2.18 mm, with 1.35 mm standard deviation (Exp N_Ex_PF and L_Ex_PF). Although there is no consensus on accuracy requirement in the literature, an error below 5 mm is considered acceptable for tumour volume larger than 0.5 ml, assuming that the tumor is spherical [45]. Also, the results are comparable with the results obtained in [17], where planar curvature tracking of PBNs was validated experimentally and 3.3 ±1.42 mm mean targeting position error was obtained with an adaptive controller. However, our error results are above the average targeting error of 1.33 mm (calculated by considering only the studies with fully-automated steering) given in [46], which reviews 8 fully-autonomous 3-D path-following studies without a PBN and an optical fiber-based localization. The main reasons for this discrepancy include: (i) tendon driven effect, which resulted in a disturbance on the tip curvature of the PBN; (ii) the lag caused by the lead-out length; (iii) the residual error resulting from the limited response speed of the ADRC to varying disturbances. In particular, the tendon driven effect is due to the friction between fibers, which are attached at the tip of the segments, and the PBN lumens.

When compared to the simulation studies in [19] and [24], which are the only 3-D PBN path-following studies in the literature, one of the key differences in these works is the timing of the PBN tip programming, which might cause significant overshoot in the case of bending angle discontinuities, as detailed in Introduction section. Conversely, we showed experimentally that our algorithm can follow a path with a significant bending angle discontinuity (90°). In addition to this, the algorithm we proposed for the PBN tip programming ensured the PBN's permissibility conditions to be observed at all times, thus resulting in the PBN acting as a single body.

In the experiments, unexpected lateral movements (up to 1 mm) of the PBN tip during PBN tip programming were detected. When a non-leading segment advances, while its tip approaches the tip of the leading segment, it pushes the leading segment laterally to create space in the tissue for itself. Conversely, when a segment is retracted away from the leading segment, the latter bounces back to the center of the channel that was previously created by the segments at the PBN tip. This behavior arises as a combination of these two reasons: (i) the non-zero friction between segments, (ii) the flexibility of the tissue and the needle. In fact, this effect could be beneficial in practice since it inherently results in an angular movement of the heading direction towards the reference path. In order to account for this effect, which was not taken into consideration during simulations, the value of the controller gain, k_p, was decreased manually for the experiments. In

addition, another unexpected behavior was seen during the *ex vivo* trials: when penetrating into different tissue layers, sometimes, the PBN partially buckled before the penetration, which caused transient disturbances in the tip curvature.

Similar to the simulation results, no considerable difference between LADRC and NADRC was detected in the experiments. In summary, LADRC is preferable in this case due to its simpler implementation.

The performance of the whole system (including sensing and control) was not assessed in this study. Rather, an FBG-based reconstruction, of which performance was already known, was considered true shape, and only the controller's performance was assessed. However, since FBG-based shape reconstruction was assumed to be the true measurement, the sensing errors were considered to be disturbances to the PBN navigation, like tissue movements, which remains one of the limitations of the approach. As future work, a medical imaging modality or a camera system could be used to eliminate this limitation and evaluate the overall system.

The proposed controller takes into account the tissue movements. The HLC defines the pseudo-target point at each time step, and if the PBN tip shifts due to a tissue movement, the HLC creates the virtual sphere with its center at the new PBN tip position. Regarding the LLC, it is often the case that employing an observer leaves a residual error since disturbance compensation is not instantaneous even when it is exact. However, in this study, the compensation was considered complete under the assumption of slow-varying disturbances, including tissue movements. This was considered an acceptable assumption, as the tissue was not expected to move abruptly with respect to the needle.

In our study, the step navigation length, m, was constrained to $m \geq$ 5 mm. However, this constraint, which was determined empirically via trial and error to achieve a reasonable insertion duration, could be optimized further, if acceptable performance could not be achieved for a given targeted path.

As per Fig. 14 and Fig. 15, the time required for the 120 mm needle insertion is approximately 4 minutes. This is mainly due to the required time for PBN tip programming at each control loop. A 4 minutes insertion duration for a 120 mm long insertion is likely to be acceptable given that the methods proposed in this study aim to eliminate tissue damage and the time required for reinsertion in the case of needle misplacement. Nevertheless, improving on this performance metric without an impact on accuracy will be the topic of future work.

Although only perturbations in position were applied at the start, the controller's performance was demonstrated to account for both position and orientation variations over the insertion length in each experiment, as the tip of the PBN took on a wide range of erroneous positions and orientations that had to be accounted for and rectified during the closed loop control process.

Finally, it is worth noting that the architecture proposed in this study and the look-ahead controller used as the HLC resemble some of the other robotic systems such as autonomous ground vehicles (e.g., autonomous tractors [47]) and underwater vehicles [48]. These systems also include an LLC to control the vehicle's maneuver.

VIII. CONCLUSION AND FUTURE WORK

In this work, path-following control methods for steerable needles using FBG-inscribed MCFs were investigated. We showed that the steerable needle localization needed for autonomous insertions can be achieved with MCFs via experimental validation of our path-following controller. To the best of our knowledge, this is the first steerable-needle path-following study utilizing MCFs with FBGs.

We also showed that the reference path can be followed at an insertion length longer than the needle length possessing FBGs without the need for extrapolation thanks to our novel FBG-based shape reconstruction method.

The NLGL has been used for guidance along the desired path. At the lower level, because of the high unpredictability of tissue-needle interactions, we proposed an ADRC-based control method because of its extreme tolerance to uncertainties, and robustness against external disturbances. With the elimination of the total disturbance, our MIMO plant was reduced to a single integration system, and only a simple linear proportional controller was used. Also, we showed experimentally, for the first time, that PBNs are suitable for autonomous 3-D path-following applications. In addition, an algorithm for PBN tip programming by observing PBN permissibility conditions was proposed. Lastly, the methods were experimentally tested both with a phantom tissue and an *ex vivo* brain tissue, and 1.79 mm mean and 6.56 mm maximum absolute position errors were obtained with 1.04 mm standard deviation.

As future work, tissue movements are planned to be observed via medical imaging methods, such as ultrasound-based methods, to detect target migration and update the path automatically. Our ongoing work also aims to measure the axial force using FBGs by reconstructing the shape simultaneously, and we plan to use it for both an emergency stop by detecting the obstacles, such as vessels, in front of the needle and detecting the target tissue layer to increase targeting accuracy. Finally, the control methods ensuring constant PBN tip velocity shall be investigated for smoother and faster navigation.

APPENDIX - STABILITY ANALYSIS OF THE LADRC

The state equations are given as follows:

$$\dot{\boldsymbol{x}}_1 = b_0\,\boldsymbol{u} + \boldsymbol{x}_2, \qquad \dot{\boldsymbol{x}}_2 = \dot{\boldsymbol{f}} \tag{19}$$

where $\boldsymbol{x}_1 = \boldsymbol{c}_t$, and $\boldsymbol{f} = \dot{\boldsymbol{\omega}}_t$.

In state space matrix form:

$$\dot{\boldsymbol{x}} = \boldsymbol{A}\boldsymbol{x} + \boldsymbol{B}\boldsymbol{u} + \boldsymbol{E}\boldsymbol{f}, \qquad \boldsymbol{y} = \boldsymbol{C}\boldsymbol{x}_1 \tag{20}$$

where

$$\dot{\boldsymbol{x}} = \begin{bmatrix} \dot{\boldsymbol{x}}_1 \\ \dot{\boldsymbol{x}}_2 \end{bmatrix}, \quad \boldsymbol{A} = \begin{bmatrix} \boldsymbol{0} & \boldsymbol{I} \\ \boldsymbol{0} & \boldsymbol{0} \end{bmatrix}, \quad \boldsymbol{B} = \begin{bmatrix} b_0\boldsymbol{I} \\ \boldsymbol{0} \end{bmatrix}$$

$$\boldsymbol{x} = \begin{bmatrix} \boldsymbol{x}_1 \\ \boldsymbol{x}_2 \end{bmatrix}, \quad \boldsymbol{C} = \begin{bmatrix} \boldsymbol{I} & \boldsymbol{0} \end{bmatrix}, \quad \boldsymbol{E} = \begin{bmatrix} \boldsymbol{0} \\ \boldsymbol{I} \end{bmatrix}$$

with $\boldsymbol{0}$ being 2×2 matrix including zeros.

Linear ESO:

$$\dot{\boldsymbol{\zeta}} = \boldsymbol{A}\boldsymbol{\zeta} + \boldsymbol{B}\boldsymbol{u} + \boldsymbol{L}(\boldsymbol{y} - \hat{\boldsymbol{y}}), \qquad \hat{\boldsymbol{y}} = \boldsymbol{C}\boldsymbol{\zeta}_1 \tag{21}$$

where $\dot{\boldsymbol{\zeta}} = \begin{bmatrix} \dot{\boldsymbol{\zeta}}_1 & \dot{\boldsymbol{\zeta}}_2 \end{bmatrix}^T$, $\boldsymbol{\zeta} = \begin{bmatrix} \boldsymbol{\zeta}_1 & \boldsymbol{\zeta}_2 \end{bmatrix}^T$, and $\boldsymbol{L} = \begin{bmatrix} \beta_1\boldsymbol{I} & \beta_2\boldsymbol{I} \end{bmatrix}^T$

For stability analysis, a method proposed in [49] is adopted here for our MIMO plant. Defining the errors, $\boldsymbol{e}_1 = \boldsymbol{x}_1 - \boldsymbol{\zeta}_1$ and $\boldsymbol{e}_2 = \boldsymbol{x}_2 - \boldsymbol{\zeta}_2$, and the error dynamics is given as follows:

$$\dot{\boldsymbol{e}} = \boldsymbol{A}\boldsymbol{e} - \boldsymbol{L}\boldsymbol{C}\boldsymbol{e} + \boldsymbol{E}\boldsymbol{f} \tag{22}$$

where $\dot{\boldsymbol{e}} = \begin{bmatrix} \dot{\boldsymbol{e}}_1 & \dot{\boldsymbol{e}}_2 \end{bmatrix}^T$, and $\boldsymbol{e} = \begin{bmatrix} \boldsymbol{e}_1 & \boldsymbol{e}_2 \end{bmatrix}^T$.

Rearranging (22):

$$\dot{\boldsymbol{e}} = \boldsymbol{A}_e\boldsymbol{e} + \boldsymbol{E}\boldsymbol{f} \tag{23}$$

where $\boldsymbol{A}_e = \boldsymbol{A} - \boldsymbol{L}\boldsymbol{C}$

Therefore, the characteristic polynomial of $\boldsymbol{A}_e$ is given as follows:

$$\begin{aligned} \lambda_c(s) &= |s\boldsymbol{I}^{4 \times 4} - \boldsymbol{A}_e| \\ &= (s^2 + \beta_1 s + \beta_2)^2 \end{aligned} \tag{24}$$

When the roots of this polynomial are on the left half-plane and h is bounded, the ESO is bounded-input bounded-output (BIBO) stable.

The closed-loop linear ADRC is represented by the state space matrix form as follows:

$$\begin{bmatrix} \dot{\boldsymbol{x}} \\ \dot{\boldsymbol{\zeta}} \end{bmatrix} = \begin{bmatrix} \boldsymbol{A} & \boldsymbol{BF} \\ \boldsymbol{LC} & \boldsymbol{A} - \boldsymbol{LC} + \boldsymbol{BF} \end{bmatrix} \begin{bmatrix} \boldsymbol{x} \\ \boldsymbol{\zeta} \end{bmatrix} + \begin{bmatrix} \boldsymbol{B} & \boldsymbol{E} \\ \boldsymbol{B} & \boldsymbol{0} \end{bmatrix} \begin{bmatrix} \boldsymbol{c}^d \\ \dot{\boldsymbol{f}}\boldsymbol{I} \end{bmatrix} \quad (25)$$

where $\boldsymbol{F} = (1/b_0) \begin{bmatrix} -k_p\boldsymbol{I} & -\boldsymbol{I} \end{bmatrix}$.

Then, the roots of the characteristic polynomial are given as $-k_p \cup \{\text{roots of (24)}\}$. Assuming that $\dot{\boldsymbol{f}}$ is bounded, and given that the reference $\boldsymbol{c}^d$ is bounded, the system is BIBO stable if all the roots are on the left half-plane.

ACKNOWLEDGMENT

REFERENCES

[1] N. Abolhassani *et al.*, "Needle insertion into soft tissue: A survey," *Medical Engineering and Physics*, vol. 29, no. 4, pp. 413–431, 2007.

[2] G. Wan *et al.*, "Brachytherapy needle deflection evaluation and correction," *Medical Physics*, vol. 32, no. 4, pp. 902–909, 2005.

[3] M. R. Prausnitz and R. Langer, "Transdermal drug delivery," *Nature Biotechnology*, vol. 26, no. 11, pp. 1261–1268, 2008.

[4] Y. Zhao *et al.*, "Evaluation and comparison of current biopsy needle localization and tracking methods using 3D ultrasound," *Ultrasonics*, vol. 73, pp. 206–220, 2017.

[5] S. Rossi *et al.*, "Percutaneous Treatment of Small Hepatic Tumors by an Expandable RF Needle Electrode," *American Journal of Roentgenology*, no. April, pp. 1015–1022, 1998.

[6] S. P. Dimaio and S. E. Salcudean, "Needle steering and motion planning in soft tissues," *IEEE Tra. Bio. Eng.*, vol. 52, no. 6, pp. 965–974, 2005.

[7] T. K. Poddler *et al.*, "Effects of Tip Geometry of Surgical Needles: An Assessment of Force and Deflection," in *The 3rd European Medical and Biological Engineering Conference*, Prague, Czech Republic, 2005.

[8] S. Misra *et al.*, "Needle-tissue interaction forces for bevel-tip steerable needles," in *2nd Biennial IEEE/RAS-EMBS Int. Conf. on Biomed. Robotics and Biomechatronics, BioRob 2008*. IEEE, 2008, pp. 224–231.

[9] P. Sears and P. Dupont, "A steerable needle technology using curved concentric tubes," in *IEEE International Conference on Intelligent Robots and Systems*, Beijing, China, 2006, pp. 2850–2856.

[10] H. B. Gilbert *et al.*, "Concentric Tube Robots as Steerable Needles: Achieving Follow-the-Leader Deployment," *IEEE Transactions on Robotics*, vol. 31, no. 2, pp. 246–258, 4 2015.

[11] R. J. Roesthuis *et al.*, "Modeling and steering of a novel actuated-tip needle through a soft-tissue simulant using Fiber Bragg Grating sensors," in *IEEE Int. Conf. on Robotics and Automation*, 2015, pp. 2283–2289.

[12] T. Watts *et al.*, "A Mechanics-Based Model for 3-D Steering of PBNs," *IEEE Transactions on Robotics*, vol. 35, no. 2, pp. 371–386, 2018.

[13] A. Majewicz *et al.*, "Design and evaluation of duty-cycling steering algorithms for robotically-driven steerable needles," *Proceedings - IEEE Int. Conf. on Robotics and Automation*, pp. 5883–5888, 2014.

[14] S. Okazawa *et al.*, "Hand-held steerable needle device," *IEEE/ASME Transactions on Mechatronics*, vol. 10, no. 3, pp. 285–296, 2005.

[15] M. C. Bernardes *et al.*, "Robot-assisted automatic insertion of steerable needles with closed-loop imaging feedback and intraoperative trajectory replanning," *Mechatronics*, vol. 23, no. 6, pp. 630–645, 2013.

[16] U. Cerkvenik *et al.*, "Mechanisms of ovipositor insertion and steering of a parasitic wasp," in *Proceedings of the National Academy of Sciences of the USA*, vol. 114, no. 37, 2017, pp. E7822–E7831.

[17] R. Secoli and F. Rodriguez y Baena, "Experimental Validation of Curvature Tracking with a Programmable Bevel-Tip Steerable Needle," in *Inter. Symposium on Medical Robotics (ISMR)*, 2018.

[18] E. Matheson *et al.*, "Cyclic Motion Control for Programmable Bevel-Tip Needle 3D Steering: A Simulation Study," in *IEEE Int. Conf. on Robotics and Biom.*, Kuala Lumpur, Malaysia, 2018, pp. 444–449.

[19] R. Secoli and F. Rodriguez y Baena, "Adaptive path-following control for bio-inspired steerable needles," in *6th IEEE RAS/EMBS Int. Conf. on Biomedical Robotics and Biomechatronics*, UTown, Singapore, 2016.

[20] D. C. Rucker *et al.*, "Sliding mode control of steerable needles," *IEEE Transactions on Robotics*, vol. 29, no. 5, pp. 1289–1299, 2013.

[21] B. Fallahi *et al.*, "Sliding-based image-guided 3D needle steering in soft tissue," *Control Eng. Practice*, vol. 63, no. April, pp. 34–43, 2017.

[22] S. Y. Ko and F. Rodriguez y Baena, "Trajectory following for a flexible probe with state/input constraints: An approach based on model predictive control," *Robotics and Autonomous Systems*, vol. 60, no. 4, pp. 509–521, 2012.

[23] B. Xu and S. Y. Ko, "3D Feedback control using fuzzy logic for a curvature-controllable steerable bevel-tip needle," *Mechatronics*, vol. 68, no. April, 2020.

[24] R. Secoli and F. Rodriguez y Baena, "Closed-loop 3D motion modeling and control of a steerable needle for soft tissue surgery," in *IEEE Int. Conf. on Robo. and Auto.*, no. 3, Germany, 2013, pp. 5831–5836.

[25] J. Han, "From PID to active disturbance rejection control," *IEEE Transactions on Industrial Electronics*, vol. 56, no. 3, pp. 900–906, 2009.

[26] R. Wang *et al.*, "Three-Dimensional Helical Path Following of an Underwater Biomimetic Vehicle-Manipulator System," *IEEE Journal of Oceanic Engineering*, vol. 43, no. 2, pp. 391–401, 2018.

[27] Y. Zhang *et al.*, "A novel control scheme for quadrotor UAV based upon ADRC," *Aerospace Science and Technology*, vol. 79, pp. 601–609, 2018.

[28] A. Donder and E. I. Konukseven, "Contour Tracking by Hybrid Force/Velocity Controlled Grinding: Comparison of Controllers ADRC -PID," in *Proc. of the World Cong. on Eng. and CS*, San Fr., USA, 2017.

[29] S. Park *et al.*, "Performance and lyapunov stability of a nonlinear path-following guidance method," *Journal of Guidance, Control, and Dynamics*, vol. 30, no. 6, pp. 1718–1728, 2007.

[30] P. B. Sujit *et al.*, "Unmanned aerial vehicle path following: A survey and analysis of algorithms for fixed-wing unmanned aerial vehicles," *IEEE Control Sys. Mag.*, vol. 34, no. 1, pp. 42–59, 2014.

[31] A. Donder and F. Rodriguez y Baena, "Kalman-Filter-Based, Dynamic 3-D Shape Reconstruction for Steerable Needles With Fiber Bragg Gratings in Multicore Fibers," *IEEE Tran. on Rob.*, vol. 38, no. 4, 2021.

[32] F. Khan *et al.*, "Pose Measurement of Flexible Medical Instruments using Fiber Bragg Gratings in Multi-Core Fiber," *IEEE Sensors J.*, 2020.

[33] J. M. Selig, "Characterisation of Frenet-Serret and Bishop motions with applications to needle steering," *Robotica*, vol. 31, no. 6, p. 981, 2013.

[34] D. G. Luenberger, "An Introduction to Observers," *IEEE Transactions on Automatic Control*, vol. 16, no. 6, pp. 596–602, 1971.

[35] J. Li *et al.*, "On asymptotic stability for nonlinear ADRC based control system with application to the ball-beam problem," *Proceedings of the American Control Conference*, vol. 2016-July, pp. 4725–4730, 2016.

[36] Z. Gao, "Active disturbance rejection control: A paradigm shift in feedback control system design," in *Proceedings of the American Control Conference*, 2006, pp. 2399–2405.

[37] A. Leibinger *et al.*, "Minimally disruptive needle insertion: a biologically inspired solution," *Interface Focus*, vol. 6, no. 3, p. 20150107, 2016.

[38] K. O. Hill and G. Meltz, "Fiber Bragg grating technology fundamentals and overview," *J. Lightwave Tech.*, vol. 15, no. 8, pp. 1263–1276, 1997.

[39] R. Xu *et al.*, "Curvature, Torsion, and Force Sensing in Continuum Robots Using Helically Wrapped FBG Sensors," *IEEE Robotics and Automation Letters*, vol. 1, no. 2, pp. 1052–1059, 2016.

[40] K. R. Henken *et al.*, "Error Analysis of FBG-Based Shape Sensors for Medical Needle Tracking," *IEEE/ASME Transactions on Mechatronics*, vol. 19, no. 5, pp. 1523–1531, 2014.

[41] R. H. Byrd *et al.*, "A trust region method based on interior point techniques for nonlinear programming," *Mathematical Programming, Series B*, vol. 89, no. 1, pp. 149–185, 2000.

[42] G. Franceschini, "The Mechanics of Human Brain Tissue," *Modell., Preserv. and Cont. of Mater. and Structures. Uni. of Trento, Italy*, 2006.

[43] C. Burrows *et al.*, "Experimental characterisation of a biologically inspired 3D steering needle," in *International Conference on Control, Automation and Systems*, Gwangju, Korea, 2013, pp. 1252–1257.

[44] S. Y. Ko *et al.*, "Closed-loop planar motion control of a steerable probe with a "programmable bevel" inspired by nature," *IEEE Transactions on Robotics*, vol. 27, no. 5, pp. 970–983, 2011.

[45] R. Seifabadi *et al.*, "Accuracy study of a robotic system for MRI-guided prostate needle placement," *Int J Med Robotics Comput Assist Surg*, no. 9, pp. 305–316, 2012.

[46] C. Rossa and M. Tavakoli, "Issues in closed-loop needle steering," *Control Engineering Practice*, vol. 62, no. January, pp. 55–69, 2017.

[47] A. González-Cantos and A. Ollero, "Backing-up maneuvers of autonomous tractor-trailer vehicles using the qualitative theory of nonlinear dynamical systems," *Int. J. of Robo. Res.*, vol. 28, no. 1, pp. 49–65, 2009.

[48] S. S. You *et al.*, "General path-following manoeuvres for an underwater vehicle using robust control synthesis," *Proc. of the Institution of Mech. Eng. Part I: J. Sys. and Cont. Eng.*, vol. 224, no. 8, pp. 960–969, 2010.

[49] Z. Gao, "Scaling and bandwidth-parameterization based controller tuning," in *Proc. American Cont. Conf., 2006.*, vol. 6, 2006, pp. 4989–4996.